Simulating the chemical enrichment of the intergalactic medium
Wiersma, R.P.C.

Citation
Wiersma, R. P. C. (2010, September 22). *Simulating the chemical enrichment of the intergalactic medium*. Retrieved from https://hdl.handle.net/1887/15972

CHAPTER 5

The enrichment history of cosmic metals

Robert P. C. Wiersma, Joop Schaye, Claudio Dalla Vecchia, C. M. Booth, Tom Theuns, and Anthony Aguirre

W$_E$ use a suite of cosmological, hydrodynamical simulations to investigate the chemical enrichment history of the Universe. Specifically, we trace the origin of the metals back in time to investigate when various gas phases were enriched and by what halo masses. We find that the age of the metals decreases strongly with the density of the gas in which they end up. At least half of the metals that reside in the diffuse intergalactic medium (IGM) at redshift zero (two) were ejected from galaxies above redshift two (three). The mass of the haloes that last contained the metals increases rapidly with the gas density. More than half of the mass in intergalactic metals was ejected by haloes with total masses less than $10^{11}\,\mathrm{M}_\odot$ and stellar masses less than $10^9\,\mathrm{M}_\odot$. The range of halo masses that contributes to the enrichment is wider for the hotter part of the IGM. By combining the 'when' and 'by what' aspects of the enrichment history, we show that metals residing in lower density gas were typically ejected earlier and by lower mass haloes.

5.1 INTRODUCTION

Despite the fact that 'metals' - heavy elements produced by stars - make up a very tiny portion of the cosmic matter budget, they are of critical importance to our understanding of the Universe. From a diagnostic point of view, they are very useful in constraining star formation and tracing feedback from massive stars and supernovae. More importantly, however, metals impact the rate at which gas cools, affecting structure formation on scales of galaxy clusters down to dust grains. This effect should not go understated since, depending on the temperature, metals can reduce the cooling time by over an order of magnitude for solar metallicity (e.g. Sutherland & Dopita 1993; Gnat & Sternberg 2007, chapter 2).

Observations clearly show that a substantial fraction of the diffuse intergalactic medium (IGM) has been enriched with heavy elements (e.g. Cowie & Songaila 1998; Schaye et al. 2000; Ellison et al. 2000; Schaye et al. 2003; Simcoe et al. 2004; Aracil et al. 2004; Schaye et al. 2007; Aguirre et al. 2008; Danforth & Shull 2008; Cooksey et al. 2010; Pieri et al. 2009). However, the physical mechanism, the timing and the sources of the enrichment all remain unknown. The IGM may have been enriched by the first generations of stars and galaxies at very high redshifts, or it may have been polluted by more massive galaxies at intermediate redshifts. Metals may be carried out into intergalactic space by galactic winds driven by supernovae, radiation pressure from star light, or by active galactic nuclei (AGN) (e.g. Cen & Ostriker 1999; Aguirre et al. 2001a,b; Madau et al. 2001; Theuns et al. 2002; Tornatore et al. 2004; Aguirre et al. 2005; Oppenheimer & Davé 2006; Davé & Oppenheimer 2007; Oppenheimer & Davé 2008; Scannapieco et al. 2006; Kawata & Rauch 2007; Kobayashi et al. 2007; Sommer-Larsen & Fynbo 2008; Shen et al. 2010; Tornatore et al. 2010; Choi & Nagamine 2010, chapter 3). In dense environments such as groups and clusters of galaxies metals may also be efficiently dispersed via processes such as ram pressure stripping or tidal stripping (see e.g. Borgani et al. 2008 for a review).

The most straightforward way to investigate when the IGM received its metals, is to plot the metallicity or metal mass as a function of redshift, as we did for a series of cosmological simulations in chapter 3. By comparing models with different physical implementations, one can obtain information about the processes that are important for IGM enrichment. However, the metals that reside in the IGM at high redshift may not be the same metals that are in the IGM at the present day. What is hot IGM gas at high redshift, may have cooled by low redshift. Intergalactic metals may also accrete onto galaxies and end up in the ISM or in stars.

Here we also use cosmological simulations to study the enrichment of the cosmos - noting that the IGM is of particular interest - but we take a novel approach in that we classify the gas based on its state at the redshift of interest (we choose $z = 0$ and $z = 2$) and trace its enrichment history back in time with the aim of understanding how the observed metals were put into place. Specifically, we will address the following two questions: When did gas that resides in the IGM at $z = 0$ and $z = 2$ receive its metals? And what are the masses of the haloes that last contained these metals?

This paper is organised as follows. In Section 5.2 we describe the simulations used, emphasising the details that are particularly pertinent here. Section 5.3 discusses *when*

the gas was enriched, taking each sub-phase in turn. In Section 5.4 we investigate *what* enriched the gas, using a halo-finder to determine what kinds of objects are mainly responsible for the enrichment of various gas phases. We connect the two ideas in Section 5.5, relating enrichment time with the last halo that contained the metals that end up in the IGM. Finally, we summarise our findings in Section 5.6.

5.2 SIMULATIONS

The simulations presented here are part of the OverWhelmingly Large Simulations (OWLS) project (Schaye et al. 2010), which consists of a large suite of cosmological, hydrodynamical simulations that include chemodynamics. We use a substantially modified version of the N-body Tree-PM, smoothed particle hydrodynamics (SPH) code GADGET III, which is itself a modified version of the code GADGET II (Springel 2005). The code includes new modules for radiative cooling and heating (chapter 2), star formation (Schaye & Dalla Vecchia 2008), chemodynamics (chapter 3), and feedback from supernovae (Dalla Vecchia & Schaye 2008). Below we will give a brief overview of the simulation ingredients that are most relevant for this work. More details can be found in Schaye et al. (2010) and the references given above.

We assume a flat ΛCDM universe with the cosmological parameters $[\Omega_m, \Omega_b, \Omega_\Lambda, \sigma_8, n_s, h, Y] = [0.238, 0.0418, 0.762, 0.74, 0.951, 0.73, 0.248]$, as determined from the WMAP 3-year data and consistent[1] with the WMAP 7-year data (Jarosik et al. 2010).

We use the radiative cooling tables presented in chapter 3[2]. In brief, net radiative cooling rates are computed element-by-element in the presence of the cosmic microwave background (CMB) and the Haardt & Madau (2001) model for the UV/X-ray background radiation from quasars and galaxies. The contributions of the eleven elements hydrogen, helium, carbon, nitrogen, oxygen, neon, magnesium, silicon, sulphur, calcium, and iron are interpolated as a function of density, temperature, and redshift from tables that have been pre-computed using the publicly available photo-ionization package CLOUDY, last described by Ferland et al. (1998), assuming the gas to be optically thin and in (photo-)ionization equilibrium.

Stars are formed from gas particles as per Schaye & Dalla Vecchia (2008). Gas at sufficiently high densities ($n_{\mathrm{H}} \gtrsim 10^{-1}\,\mathrm{cm}^{-3}$) is expected to be multiphase and star-forming (Schaye 2004). Because we lack the resolution and the physics to model the cold interstellar phase, we impose an effective equation of state with pressure $P \propto \rho_{\mathrm{g}}^{4/3}$ for densities exceeding $n_{\mathrm{H}} = 0.1\,\mathrm{cm}^{-3}$, normalised to $P/k = 1.08 \times 10^3\,\mathrm{cm}^{-3}\,\mathrm{K}$ at the threshold. For this slope of the equation of state both the Jeans mass and the ratio of the Jeans length and the SPH kernel are independent of the density, thus preventing spurious fragmentation due to a lack of numerical resolution. Star-forming gas particles are stochastically converted into star particles at a pressure-dependent rate that is determined analytically from the observed Kennicutt-Schmidt star formation law.

---

[1]The most significant discrepancy is in σ_8, which is 8% lower than the value favoured by the WMAP 7-year data.

[2]We used their equation (3) rather than (4) and CLOUDY version 05.07 rather than 07.02.

Supernova feedback is injected in kinetic form, as described in Dalla Vecchia & Schaye (2008). After a short delay of $t_{SN} = 3 \times 10^7$ yr, corresponding to the maximum lifetime of stars that end their lives as core-collapse supernovae, newly-formed star particles inject kinetic energy into their surroundings by kicking a fraction of their neighbours in a random direction. The reference simulations presented here use the default parameters of Dalla Vecchia & Schaye (2008), which means that each SPH neighbour i of a newly-formed star particle j has a probability of $\eta m_j / \sum_{i=1}^{N_{ngb}} m_i$ of receiving a kick with a velocity v_w, where $N_{ngb} = 48$ is the number of SPH neighbours. We choose $\eta = 2$ and $v_w = 600$ km s^{-1} (i.e. if all baryonic particles had equal mass, each newly formed star particle would kick, on average, two of its neighbours). Assuming that each star with initial mass in the range $6 - 100$ M$_\odot$ injects 10^{51} erg of kinetic energy, these parameters imply that the total wind energy accounts for 40 per cent of the available kinetic energy for a Chabrier IMF and a stellar mass range $0.1 - 100$ M$_\odot$ (if we consider only stars in the mass range $8 - 100$ M$_\odot$ for type II supernovae, this works out to be 60 per cent). The value $\eta = 2$ was chosen to roughly reproduce the peak in the cosmic star formation rate (see Schaye et al. 2010).

For the chemo-dynamics, we employ the method described in chapter 3. We use a Chabrier (2003) stellar initial mass function, with mass limits of 0.1 M$_\odot$ and 100 M$_\odot$. We consider enrichment due to mass loss from AGB and massive stars as well as type Ia and II supernovae (SNIa and SNII respectively). Our prescription for stellar evolution is heavily based on the Padova models as we use the lifetimes of Portinari et al. (1998) and the yields of low mass and high mass stars of Marigo (2001) and Portinari et al. (1998), respectively. The yields of Portinari et al. (1998) include ejecta from SNII along with estimates of mass loss from high mass stars. Using these yields gives an element of consistency between the low and high mass stars. Finally, we use the 'W7' SNIa yields of Thielemann et al. (2003).

As the precise channels of SNIa progenitors are uncertain, we employ SNIa explosion rates that roughly reproduce the observed cosmic SNIa rate. We note that the observations from different surveys are not consistent and that our rates conform to the most recent data. An e-folding delay time is used to describe the SNIa rate and we use a corresponding efficiency (i.e. number of white dwarfs that become SNIa) of 2.5%.

We use SPH-smoothed metallicities for cooling and stellar evolution purposes, where $Z_{sm} \equiv \rho_Z / \rho_g$ for gas particles, and star particles inherit the smoothed metallicities of their progenitors. In chapter 3 we argued that this definition is more consistent with the SPH formalism than the more commonly used particle metallicity, $Z_{part} \equiv m_Z / m_g$. Using smoothed metallicities results in a spreading of metals over greater volumes, increasing the average rates of cooling and star formation.

Since SPH is a Lagrangian scheme, metals move with the particles they are attached to, and hence a high-metallicity particle may in principle be completely surrounded by low-metallicity gas. Introducing smoothed metallicities partially mitigates this numerical artefact. However, SPH codes may underestimate the true amount of gas mixing as compared to grid codes in case of instabilities (Agertz et al. 2007) or turbulence (Mitchell et al. 2009). It would thus be very interesting to investigate whether the metal distribution in such grid simulations is similar to that obtained with SPH. On

Table 5.1: List of simulations. From left-to-right the column show: simulation identifier, dark matter particle mass, baryonic particle mass, maximum physical gravitational softening (the softening is held fixed in comoving coordinates above $z = 2.91$), final redshift, and a brief description.

Simulation	$m_{\rm dm}$ $(h^{-1}\,{\rm M_\odot})$	$m_{\rm b}$ $(h^{-1}\,{\rm M_\odot})$	$\epsilon_{\rm prop}$ $(h^{-1}\,{\rm kpc})$	$z_{\rm end}$	Comment
L025N512	6.3×10^6	1.4×10^6	0.5	1.45	Reference model
L050N512	5.1×10^7	1.1×10^7	1.0	0	Reference model
L025N256	5.1×10^7	1.1×10^7	1.0	2	Reference model
L050N256	4.1×10^8	8.7×10^7	2.0	0	Reference model
L100N512	4.1×10^8	8.7×10^7	2.0	0	Reference model
AGN_L100N512	4.1×10^8	8.7×10^7	2.0	0	Includes AGN
WDENS_L100N512	4.1×10^8	8.7×10^7	2.0	0	Wind vel. prop. to local sound speed (SN energy as *REF*)

the other hand, we note that Shen et al. (2010) included turbulent diffusion of metals in cosmological SPH simulations but found its effect to be small.

Of the OWLS suite of simulations (described in Schaye et al. 2010), we use the subset listed in Table 5.1. Here we make use of the notation *LXXXNYYY*, where the simulation cube has a comoving side length of XXX $h^{-1}\,{\rm Mpc}$ and uses YYY^3 dark matter particles and YYY^3 baryonic particles. Table 5.1 also lists the dark matter and the initial baryonic particle masses, $m_{\rm dm}$ and $m_{\rm b}$, the maximum proper gravitational softening (the softening is fixed to this value in comoving coordinates above $z = 2.91$), $\epsilon_{\rm prop}$, the redshift at which the simulation was stopped, $z_{\rm end}$, and a short description.

We explore two variations on the reference model (*REF*). Run *AGN_L100N512* includes the prescription of Booth & Schaye (2009) for the growth of supermassive black holes by gas accretion and mergers, and for feedback from AGN. The black holes inject 1.5 per cent of the accreted rest mass energy as thermal energy in the surrounding interstellar medium. This model reproduces not only the the local black hole scaling relations (Booth & Schaye 2009), but also the observed entropy, temperature, and metallicity profiles of groups of galaxies and the stellar masses that they contain (McCarthy et al. 2009).

For run *WDENS_L100N512* the parameters of the winds are dependent on the local density, keeping the energy per unit stellar mass formed constant. They scale such that in high-density environments the wind velocity is higher:

$$v_{\rm w} = v_{\rm w}^* \left(\frac{n_{\rm H}}{n_{\rm H}^*} \right)^{1/6}, \tag{5.1}$$

$$\eta = \eta_* \left(\frac{n_{\rm H}}{n_{\rm H}^*} \right)^{-1/3}, \tag{5.2}$$

where $v_{\rm w}^* = 600\,{\rm km\,s^{-1}}$ and $\eta_* = 2$ such that the model agrees with the reference model at the threshold for star formation. For higher gas pressures the velocity increases in
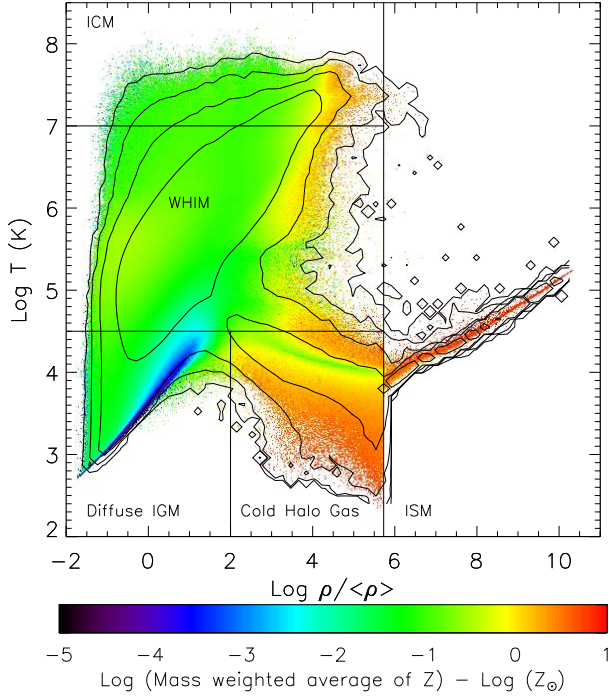
Figure 5.1: Mass weighted metal distribution in temperature-density space at $z = 0$ in simulation *L050N512*. The colour scale gives the metallicity. The contours indicate the metal mass distribution and are logarithmically spaced by 1 dex. The straight lines indicate the adopted division of the gas into: non-star-forming gas (i.e., $n_{\rm H} < 0.1\ {\rm cm}^{-3}$), diffuse photo-ionised IGM ($\rho < 10^2 \langle \rho \rangle$, $T < 10^{4.5}\ {\rm K}$), cold halo gas ($\rho > 10^2 \langle \rho \rangle$, $T < 10^{4.5}\ {\rm K}$), WHIM ($10^{4.5}\ {\rm K} < T < 10^7\ {\rm K}$), and ICM ($T > 10^7\ {\rm K}$). The metals are distributed over a wide range of densities and temperatures.

proportion with the local sound speed. Schaye et al. (2010) find that this model is much more efficient at suppressing star formation in massive galaxies, though not as efficient as the model that includes AGN.

5.3   WHEN WAS THE GAS ENRICHED?

In this section we will investigate how the time at which a gas element was enriched varies with its density and temperature at some later time. We will evaluate the enrichment history of the gas as a function of its physical state at both $z = 0$ and $z = 2$. Before doing so, it is, however, instructive to look at the distribution of metal mass at the present time, which we show in Fig. 5.1.

Fig. 5.1 indicates how we can divide the temperature-density plane in several regions of interest. For $n_{\rm H} > 0.1\ {\rm cm}^{-3}$ (which corresponds to $\rho/\langle \rho \rangle > 5.3 \times 10^5$ at $z = 0$ and $\rho/\langle \rho \rangle > 2.0 \times 10^4$ at $z = 2$) we impose an effective equation of state and assume the gas to be star-forming. We divide the non-star-forming gas into hot gas typically found in haloes of large groups or clusters (ICM, $T > 10^7\ {\rm K}$), warm-hot intergalactic gas (WHIM, $10^{4.5}\ {\rm K} < T < 10^7\ {\rm K}$), diffuse photo-ionised IGM ($\rho < 10^2 \langle \rho \rangle$, $T < 10^{4.5}\ {\rm K}$), and cold halo gas ($\rho > 10^2 \langle \rho \rangle$, $T < 10^{4.5}\ {\rm K}$). While we have divided the cold ($T < 10^{4.5}\ {\rm K}$) gas into low- and high-density components (diffuse IGM and cold halo gas, respectively), we have not done the same for hotter gas. We find that if we split the WHIM at $\rho = 10^2 \langle \rho \rangle$, the enrichment history of the low-density component is very similar to that of the WHIM in total, whereas that of the high-density component is more similar to the enrichment history of the ICM. The high-density component contains less than

Table 5.2: Fractional distribution of metals in the reference models at $z = 0$ and $z = 2$.

Phase	Fraction of metals (%)
L050N512 ($z = 0$)	
Stars	68.2
SF Gas	5.8
ICM	1.3
WHIM	19.0
Cold Halo Gas	4.6
Diffuse IGM	1.0
L025N512 ($z = 2$)	
Stars	42.0
SF Gas	25.8
ICM	< 0.1
WHIM	24.0
Cold Halo Gas	7.2
Diffuse IGM	0.9

one quarter of the WHIM metals at $z = 0$ and less than one sixteenth at $z = 2$.

In chapter 3 we showed that the metallicities predicted for these phases[3] by our reference model are in agreement with the observations, although the metallicity for the diffuse IGM may be slightly too low and is not yet fully converged with respect to the numerical resolution (it increases with increasing resolution).

The contours in Fig. 5.1 show how the metal mass is distributed in temperature-density space. The metals are spread over a wide range of phases. The metallicity (that is, the ratio of metal mass to total mass), indicated by the colour scale, ranges significantly between the various regions. That the contours do not always trace the regions with the highest metallicities highlights the fact that the metals are distributed rather differently from the rest of the baryons. Table 5.2 summarises the $z = 0$ and $z = 2$ metal mass distributions for the reference model.

We will make frequent use of what we will term "metal-mass-weighted mean red-shifts", z_Z. This quantity, which we compute on the fly for all gas particles in our simulations, is defined as the mean redshift of enrichment events weighted by the metal mass imparted by each event:

$$z_Z \equiv \frac{\sum_i \Delta m_{Z;i} z_i}{m_Z}, \tag{5.3}$$

where $\Delta m_{Z;i}$ is the metal mass received by the gas particle at redshift z_i (i indicates a time-step) and m_Z is the total metal mass of the particle. Thus, if a gas particle received all its metals over a short interval (which is typical for particles that have been ejected from haloes), this quantity gives the redshift at which it was enriched. Note that z_Z does not correspond to the time at which the metals were created. Stars may create metals long before they are released and metals may be cycled through multiple

---

[3]Note that in chapter 3 we used $T = 10^5$ K as the dividing temperature for WHIM and cold gas; we lower the limit here so that we can better isolate the components visible in Fig. 5.2.

generations of stars. We will nevertheless sometimes refer to the metals residing in gas with higher values of z_Z as being "older". In §5.4 we will show that for intergalactic metals z_Z is typically close to the redshift at which the metals last resided in a halo.

Fig. 5.2 shows z_Z in temperature-density space for *L050N512* at $z = 0$ (left panel) and for *L025N512* at $z = 2$ (right panel). Note that this figure contains no information about how much metal mass is actually in a given bin (for instance, the diffuse IGM contains relatively little metal mass, but this is not obvious from this plot). We can, however, refer back to Fig. 5.1 to see the metal distribution. For reference, computing the metal mass weighted average over all gas (stars) yields $z_Z \approx 1.5$ ($z_Z \approx 1.2$) for *L050N512* at $z = 0$ and $z_Z \approx 3.1$ ($z_Z \approx 3.2$) for *L025N512* at $z = 2$.

The most prominent trend visible in Fig. 5.2 is a strong overall gradient with density, with higher density gas being enriched more recently. This agrees with the predictions of Oppenheimer & Davé (2009) for the low-redshift, diffuse IGM as traced by O VI absorbers. Of all components, the star-forming gas (i.e., the ISM) has been enriched most recently. This is not unexpected, as this is the gas that surrounds the stars that are releasing the metals. Moreover, much of the metal mass that was injected into the ISM a long time ago, will already have been locked up in stars. Indeed, the metals locked up in stars were, on average, released (by other, older stars) earlier than the metals that reside in the ISM as can be seen by comparing the colour of the rectangles in the bottom-right parts of the panels to that of the ISM. The fact that the increase of z_Z with decreasing density continues all the way to the lowest densities, suggests that travel-time is a limiting factor for the enrichment of the IGM, as suggested by Aguirre et al. (2001b).

Fig. 5.2 also reveals some interesting trends with the gas temperature. For high gas densities, the dependence on temperature reflects a dependence on the radiative cooling time. We can see this by comparing to the solid and dashed contours, which show where the net radiative cooling time[4], t_{cool}, equals the Hubble time, t_{H}, for gas with solar and primordial abundances, respectively. The two contours that enter the diagram at high and low temperatures correspond to net cooling and heating, respectively. They converge at high densities and intermediate temperatures at the equilibrium temperature. There the contours should really extend further to the bottom right, approximately to the star formation threshold (above which we impose an effective equation of state), but they stop due to the finite resolution of the grid on which we have computed the cooling time. Gas to the right of the contours has $t_{\mathrm{cool}} < t_{\mathrm{H}}$, but gas to the left of the contours cannot cool. Clearly, the enrichment redshift is a decreasing function of the cooling time if $t_{\mathrm{cool}} < t_{\mathrm{H}}$. Since the gas cannot remain in the same area of the temperature-density plane for more than a cooling time, this implies that the time since enrichment is correlated with the time since the gas parcel moved significantly in the $T - \rho$ diagram. This is for example expected if the gas was enriched and shock-heated at roughly the same time, as in a galactic wind. It would, however, also happen if the enrichment led to a strong reduction in the cooling time.

In the long cooling time regime (i.e. to the left of the contours) the enrichment red-

---

[4]We plot only the radiative cooling time, but note that the actual cooling rates in the simulation are dominated by adiabatic expansion for low densities.
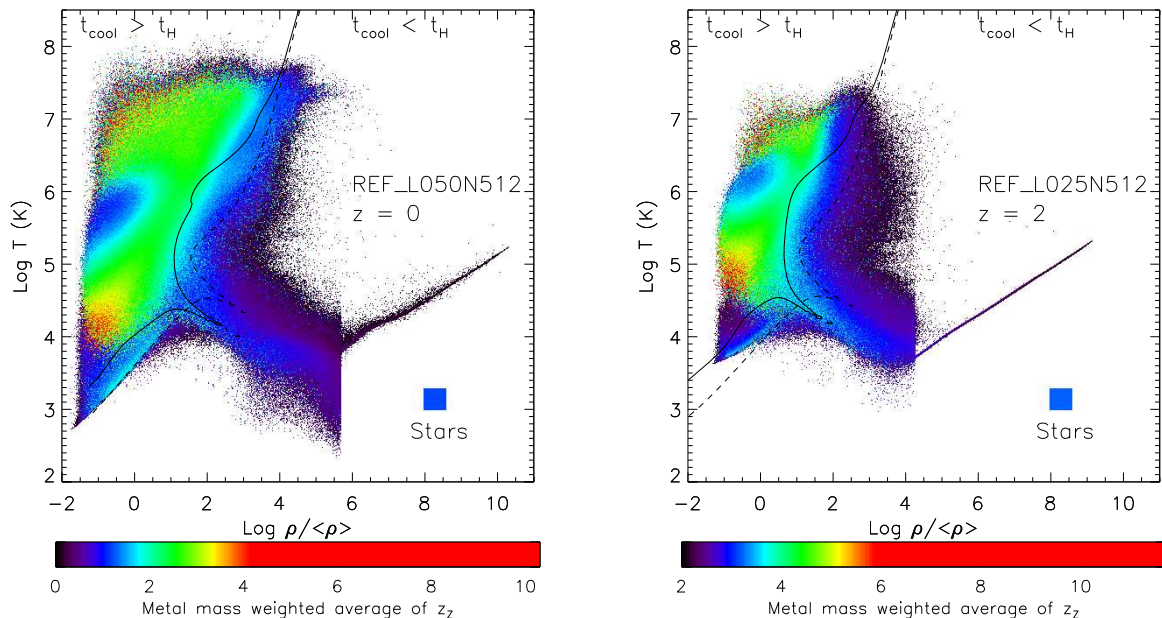
Figure 5.2: Enrichment redshift in temperature-density space. The colour scale gives the metal mass weighted mean enrichment redshift as a function of the gas density and temperature at $z = 0$ in *L050N512* (left panel) and at $z = 2$ in *L025N512* (right panel). Each pixel shows the metal mass weighted average value of z_Z for all particles that fall into the corresponding temperature-density bin. The rectangles in the bottom-right parts of the diagrams indicate the corresponding values for the metals locked up in stars. Also plotted are $t_{\mathrm{cool}} = t_{\mathrm{H}}$ contours for solar (solid) and primordial (dashed) abundances. Note that we have stretched the colour scale to emphasise the different components (only a handful of pixels correspond to high values of z_Z) and that the two panels use different colour scales. Denser gas was typically enriched later. The enrichment redshift is particularly small for gas with a short cooling time.

shift also depends on the gas temperature. We will show later (see Fig. 5.3) that some of the features for $\rho \lesssim \langle \rho \rangle$ and $T > 10^4\,\mathrm{K}$ are sensitive to the implementation of feedback. However, the finding that the coldest part of the diffuse IGM was enriched more recently than the WHIM, is robust. Note, however, that the diffuse IGM contains very few metals compared to the WHIM (see Fig. 5.1). We will show in section 5.4 (Fig. 5.11) that most of the metals in the cold, underdense part of the diffuse IGM have never been part of a (resolved) halo. This suggests that this gas may have been enriched by winds from intermediate-mass, intergalactic stars (presumably formed in galaxies and then ejected). Apparently, gas that has been enriched and ejected by galactic winds ends up in the WHIM at higher temperatures, probably because it has been put onto a higher adiabat as a result of shock-heating. Once the gas has entered the region where $t_{\mathrm{cool}} > t_{\mathrm{H}}$, it can no longer decrease its entropy, preventing low-density WHIM gas from moving into the diffuse, photo-ionised region of the diagram.

The left panel of Fig. 5.3 shows $z_Z(T, \rho)$ at $z = 0$ for the *L100N512* version of the reference model. Comparison with the left panel of Fig. 5.2, which showed the prediction for a simulation with 8 (2) times higher mass (spatial) resolution shows that the trends have converged numerically.
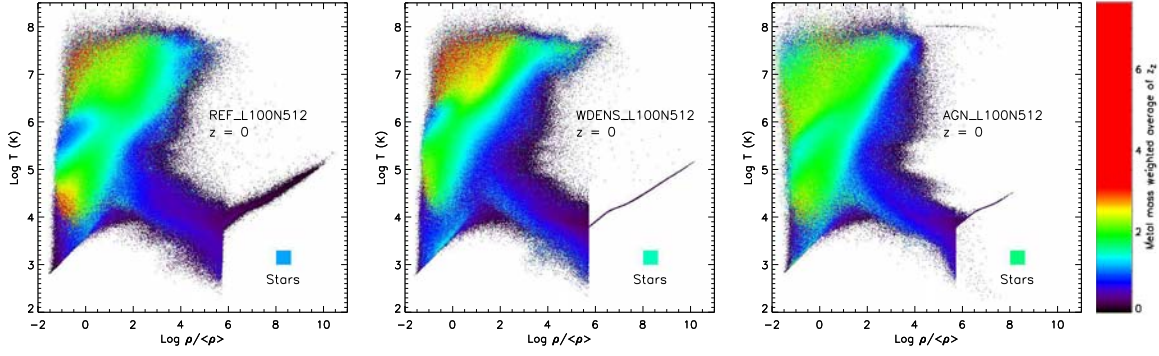
Figure 5.3: A comparison of the enrichment redshifts for simulations including different feedback processes. The colour scale gives the metal mass weighted mean enrichment redshift as a function of the gas density and temperature at $z = 0$ for simulations *REF_L100N512* (left panel), *WDENS_L100N512* (middle panel), and *AGN_L100N512* (right panel). Model *WDENS* uses an implementation of supernova-driven winds that is more efficient in massive haloes than that of model *REF*. Model *AGN* uses the same prescription for supernova feedback as model *REF*, but includes feedback from AGN. The rectangles in the bottom-right parts of the diagrams indicate the values of z_Z for the metals locked up in stars. For numerical reasons that are explained in the main text, the unresolved multiphase ISM (Log $\rho/\langle\rho\rangle \gtrsim 6$) follows a much tighter equation of state for models *WDENS* and *AGN* than for model *REF*. While the features seen at $(\rho, T) \sim (10^{-1} \langle\rho\rangle, 10^{4.3}\,\mathrm{K})$ and $(10^{-0.5} \langle\rho\rangle, 10^{5.7}\,\mathrm{K})$ for model *REF* depend on the implementation of galactic winds, the other trends are robust.

The remaining panels of Fig. 5.3 show the enrichment redshift predicted by two other simulations from the OWLS project. The middle panel shows model *WDENS*, for which the wind velocity scales with the local sound speed, while keeping the total energy per unit stellar mass identical to that used in model *REF*. In this model the supernova driven winds remain efficient up to higher halo masses, which results in a lower global star formation rate at low redshift (Schaye et al. 2010). The right panel shows the results for model *AGN*, which uses the same prescription for supernova feedback as model *REF*, but which also includes feedback from accreting supermassive black holes. Since AGN feedback is most relevant for high halo masses, the star formation rate, and thus the rate at which metals are both produced and locked up in stars, decreases much faster below $z = 2$ than for the other models (Schaye et al. 2010). This explains the increase in the metal mass weighted mean enrichment redshift of the stars, from $z_Z \approx 1.1$ for model *REF* to 1.5 for *WDENS* to 1.6 for *AGN* (the corresponding values for the gas are $z_Z \approx 1.1$, 1.3, and 1.5, respectively).

The gas on the equation of state (Log $\rho/\langle\rho\rangle \gtrsim 6$), which represents the unresolved, multiphase ISM, displays much less scatter for *WDENS* and *AGN* than for *REF*. This reflects the fact that for the latter model the output time corresponded to a global time-step whereas passive particles were caught 'drifting' adiabatically between time-steps in the reference run, resulting in temperatures that deviate slightly from our imposed equation of state. Note that this does not represent any difference in how the hydrodynamical forces were calculated among the three simulations. Observe also that some of the particles in the right panel fall on a line near $10^8\,\mathrm{K}$. This corresponds to the AGN

heating temperature (see Booth & Schaye 2009) and thus implies that these particles have been heated very recently.

Comparing the three panels, we see that the features seen at $(\rho, T) \sim (10^{-1} \langle \rho \rangle,$ $10^{4.3} \, \mathrm{K})$ and $(10^{-0.5} \langle \rho \rangle, 10^{5.7} \, \mathrm{K})$ for model *REF* depend on the implementation of supernova-driven winds. All other trends of z_Z with T and ρ are, however, robust. Even AGN feedback does not change the trends discussed above. Since the differences between the simulations are small compared to the similarities, we will only make use of our higher resolution reference model for the remainder of this section. It should be kept in mind, however, that this model probably underestimates the typical enrichment redshift due to the absence of an efficient feedback mechanism in massive galaxies.

Figs. 5.2 and 5.3 do not allow us to infer what the typical enrichment time is of metals as a function of just density or just temperature, because the diagrams do not take into account the distribution of metal mass in the $T - \rho$ plane. The solid curves in Fig. 5.4 therefore show the metal mass weighted mean enrichment redshift as a function of density (left panel) or temperature (right panel). The black and red curves show results for *L050N512* at $z = 0$ and for *L025N512* at $z = 2$, respectively.

Focusing first on the left panel, we see strong gradients with the gas density. While gas that is diffuse at $z = 0$ was typically enriched at $z \approx 2$, metals that reside in collapsed structures (i.e. $\rho \gtrsim 10^2 \langle \rho \rangle$) at the present time, were on average released much more recently. The enrichment redshift continues to decrease down to the highest densities. The same holds at $z = 2$, although the gradient is less steep at high densities. Gas that is diffuse at $z = 2$ typically received its metals at $z > 3$ and metals residing in underdense gas at $z = 2$ were on average ejected at $z > 4$.

Similarly, the right panel of Fig. 5.4 shows the metal mass weighted enrichment redshift as a function of the gas temperature at $z = 0$ (black) and $z = 2$ (red) for all gas (solid) as well as for gas with density smaller (dot-dashed) or greater (dashed) than $10^2 \langle \rho \rangle$. The enrichment redshift peaks for $T \sim 10^5 - 10^6 \, \mathrm{K}$, but this merely reflects the more fundamental trend with density: metals in this temperature range mostly reside in diffuse gas while lower and higher temperatures are dominated by higher densities.

So far we have only plotted the metal mass weighted enrichment redshift averaged over all gas particles in some temperature and/or density bin. Such plots do not reveal information about the distribution in the values of z_Z of the particles that fall into the bin. Fig. 5.5 provides this information by plotting the metal mass weighted cumulative probability distribution function of z_Z. In other words, it shows the fraction of the metal mass that resides in gas particles for which z_Z exceeds the value that is plotted along the x-axis. The different columns and line styles show the different regions in $T - \rho$ space defined in Fig. 5.1 and the different colours correspond to different resolutions. The top and bottom rows are for $z = 0$ and 2, respectively.

Fig. 5.5 shows that the metals residing in a particular gas phase typically span a wide range of enrichment redshifts. Note that this plot underestimates the true range, because it shows the distribution of z_Z for gas particles, which have themselves been averaged over all past enrichment events (weighted by metal mass). That is, even though a particle may have experiences multiple enrichment events, it only has a single
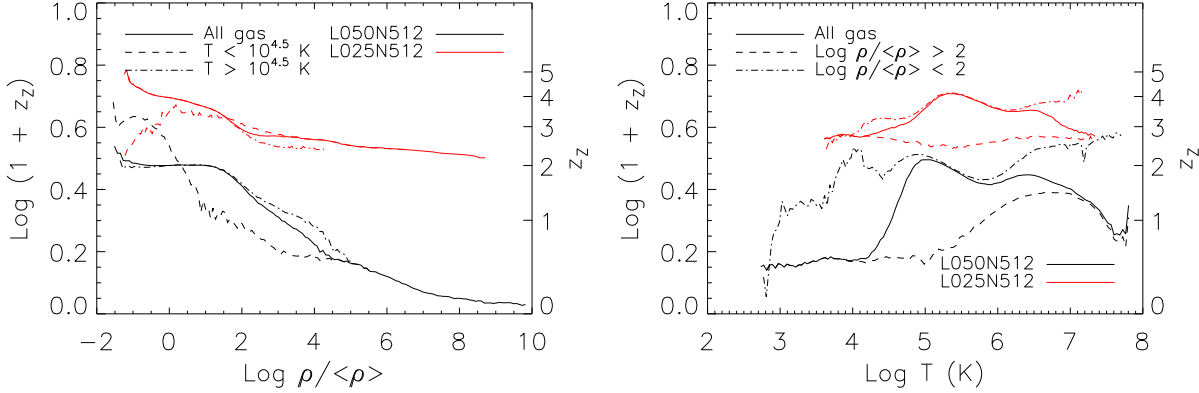
Figure 5.4: Metal mass weighted mean enrichment redshift as a function of the gas density (left panel) or the gas temperature (right panel) at $z = 0$ for model *L050N512* (black) and at $z = 2$ for *L025N512* (red). The different line styles correspond to cuts in the temperature (left panel) or density (right panel) as indicated in the legends. The curves were cut when the number of particles per bin falls below 200. The enrichment redshift decreases rapidly with increasing density. Metals residing in gas with intermediate temperatures ($T \sim 10^5 - 10^6$ K) are typically older, but this merely reflects the fact that metals at these temperatures reside mostly in lower density gas than metals at lower or higher temperatures, as can be seen by comparing the different line styles in the right panel.

value of z_Z. The distribution is particularly wide if the average enrichment redshift is high. While the average value of z_Z is about 2 for the diffuse IGM at $z = 0$, a quarter of the metal mass resides in particles with $z_Z < 1$ and another quarter has $z_Z > 3$.

Comparison of the different line colours shows that the convergence with numerical resolution is excellent for stars, the ISM, cold halo gas, and the ICM, but that it is less good for the diffuse IGM and the WHIM, particularly at $z = 0$. It is likely that our highest resolution simulation at this redshift, *L050N512*, still significantly underestimates the typical enrichment redshift of these low-density components. We will show in the next section that this is because low-mass haloes dominate the enrichment of low-density gas.

5.4 HOW MASSIVE WERE THE OBJECTS THAT ENRICHED THE GAS?

Now that we have a general impression of when the cosmic gas was enriched, we would like to investigate what types of galaxies were responsible for the enrichment. That is, do galaxies residing in certain halo masses preferentially enrich a typical phase of gas? We will address this question by determining the mass of the halo from which the metals were last ejected.

We identify haloes using a friends-of-friends group finder with a linking length of 0.2. This group finder is run on the dark matter particles in the simulation. Baryonic
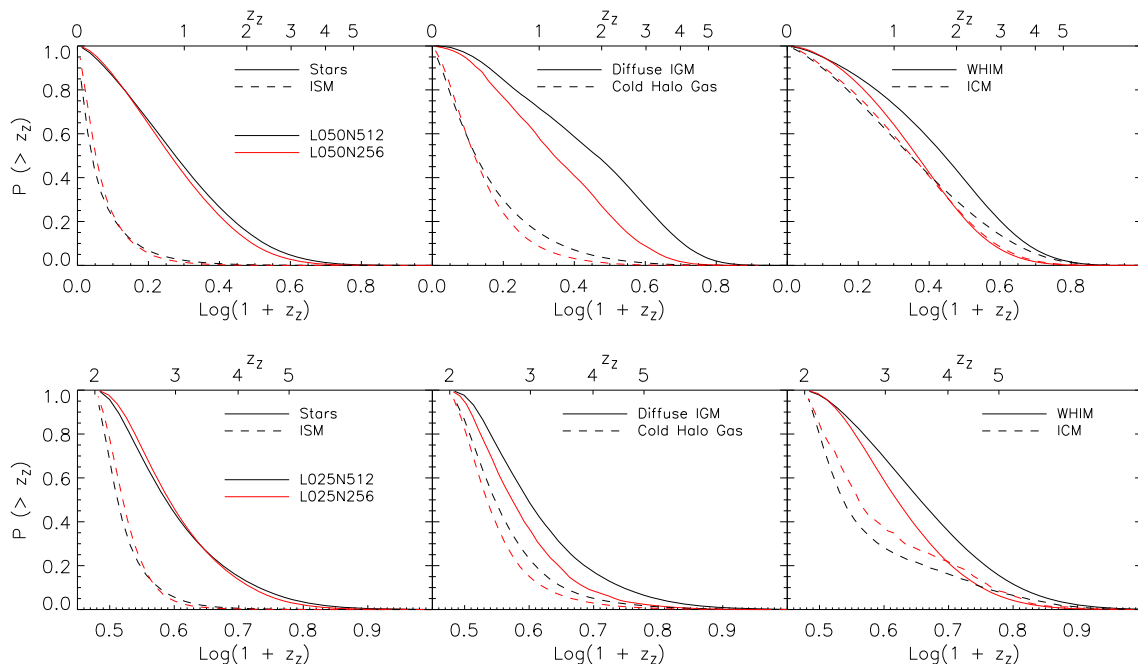
Figure 5.5: Cumulative probability distribution of the enrichment redshift, weighted by metal mass, of metals at $z = 0$ (top row) and $z = 2$ (bottom row) for stars and for the different gas phases defined in Fig. 5.1. The different colours correspond to different numerical resolutions. The results are converged with respect to resolution except for the diffuse IGM and the WHIM. For this gas even our highest resolution runs may underestimate the enrichment redshift. There is substantial scatter in the enrichment redshift, particularly for the phases whose metals are, on average, older.

particles are associated with their nearest dark matter neighbour. We include only haloes with at least 100 dark matter particles, because we found that this limit results in excellent agreement with the Sheth et al. (2001) fit to the dark matter halo mass function. For model *L100N512* this lower limit corresponds to a typical $z = 0$ stellar mass of $\sim 10^{9.0} \, \mathrm{M}_\odot$ and this is also roughly the value below which the stellar mass function cuts off due to the limited resolution. For models *L050N512* and *L025N512*, however, the stellar mass already cuts off below about $10^{2.5}$ dark matter particles, which corresponds to stellar masses of $\sim 10^{8.3} \, \mathrm{M}_\odot$ for *L050N512* at $z = 0$ and $\sim 10^{7.7} \, \mathrm{M}_\odot$ for *L025N512*. We therefore expect that we will underestimate the importance of the lowest mass haloes that we consider, particularly for these last two models.

To make the connection between metals and the haloes out of which they were ejected, we perform the following calculation. For each enriched particle, we begin at $z = 0$ ($z = 2$ for the *L025N512* simulation) and search for that particle (using its unique ID) in the friends-of-friends halo catalogue. If said particle is found, we note the total mass of the halo (m_{halo}), and the corresponding redshift, z_{halo}. For all particles not found in this output, we choose halo outputs at successively higher redshifts[5], until we

---

[5]Halo catalogues were generated at all simulation output redshifts. These are spaced at $\Delta z = 0.125$
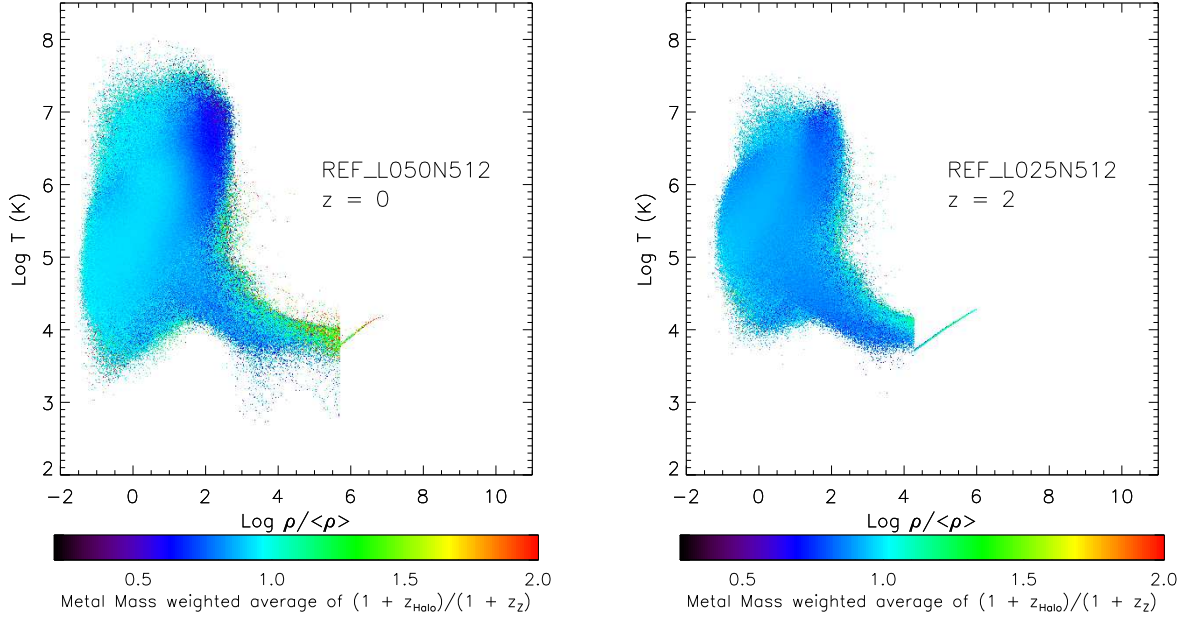
Figure 5.6: Ratio of $(1+z_{\mathrm{halo}})/(1+z_Z)$ as a function of gas density and temperature in *L050N512* at $z = 0$ (left panel) and at $z = 2$ for *L025N512* (right panel). Only gas that is not currently part of a resolved halo is included. The metal mass weighted mean enrichment redshift, z_Z, is typically similar to, but slightly higher than z_{halo}, the metal mass weighted mean redshift at which the metals last resided in a resolved halo. This implies that the gas was ejected from the halo shortly after it was enriched.

have exhausted all of them. For every particle we thus have values for the temperature, density, and metal mass as well as z_{halo} and m_{halo} (unless no corresponding halo is found in our outputs). Note that the temperature and density recorded are for $z = 0$ (or $z = 2$), whereas m_{halo} is the mass of the host halo at redshift z_{halo}.

Before showing the results of such calculations, we investigate the relation between the metal mass weighted enrichment redshift, z_Z, and z_{halo} for gas that has been part of, but that is not currently in, a resolved halo. If metals in the IGM were ejected from the haloes in which they formed shortly after they were released by stars, then the two redshifts should roughly agree. We would expect the two to be similar, as both metal enrichment and outflows are driven by massive stars, with z_{halo} somewhat smaller than z_Z, simply because it takes some time for gas that has been ejected to reach the virial radius and leave the halo. However, even if enrichment and ejection happen nearly simultaneously, we would expect differences of the order of the time scales corresponding to the time intervals between snapshots. Fig. 5.6 shows that z_{halo} and z_z do indeed agree very well for almost all temperatures and densities. This is true for both $z = 0$ and $z = 2$. An exception is hot, dense gas ($10^6 \mathrm{K} \lesssim T \lesssim 10^7 \mathrm{K}, \rho \sim 10^2 \langle \rho \rangle$) at $z = 0$, for which z_{halo} is significantly smaller than z_Z. This may be because this gas recently moved from the ICM across (our definition of) the halo boundary, but was

for $0 \leq z \leq 0.5$, at $\Delta z = 0.25$ for $0.5 \leq z \leq 4$, and at $\Delta z = 0.5$ for $4 \leq z \leq 9$. We also have outputs for $z = 10, 12.5, 15$, and 20.
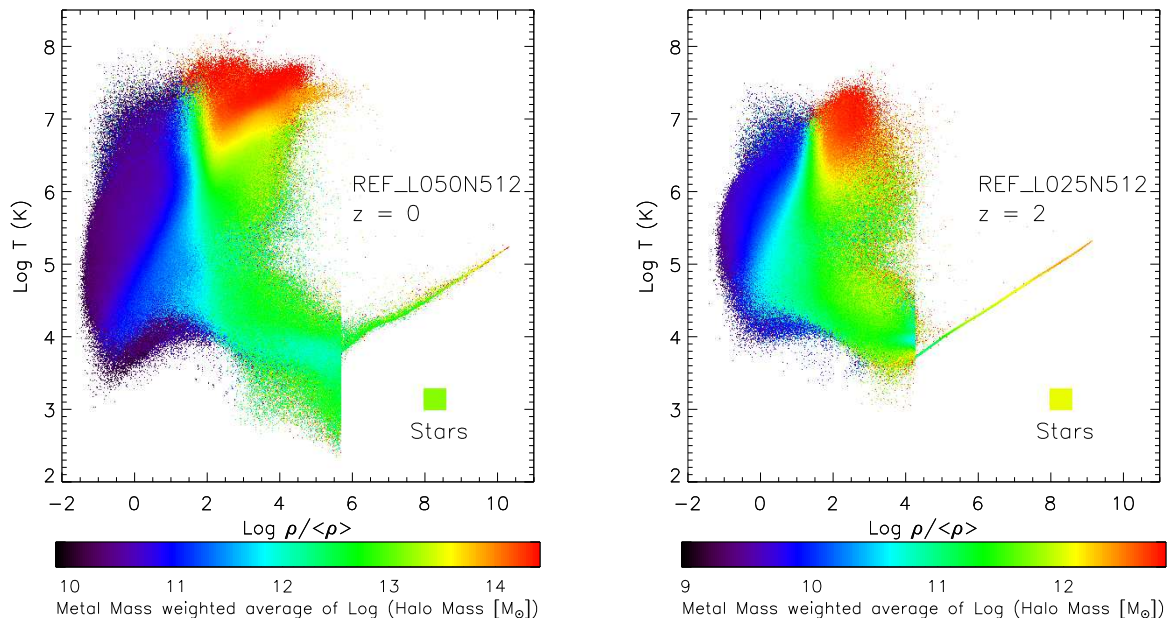
Figure 5.7: Metal mass weighted mean $\log_{10} m_{\mathrm{halo}}$, where m_{halo} is the total mass of the halo that last contained the metals, as a function of the gas density and temperature at $z = 0$ in *L050N512* (left panel) and at $z = 2$ in *L025N512*. Each pixel shows the metal mass weighted average value of $\log_{10} m_{\mathrm{halo}}$ for all particles that fall into the corresponding temperature-density bin. The rectangles in the bottom-right parts of the diagrams indicate the corresponding values for the metals locked up in stars. Only particles that have resided in haloes with more than 100 dark matter particles are included. Note that the two panels use different colour scales. Metals residing in lower density gas originate from lower mass haloes. Because high-density gas ($\rho \gtrsim 10^2 \langle \rho \rangle$) currently resides in haloes, the increase in halo mass with temperature reflects their virial temperatures. The diffuse IGM is nearly completely missing from this plot because it is enriched by unresolved haloes and/or intergalactic stars.

enriched at relatively high redshift. Note that gas with $\rho \gtrsim 10^2 \langle \rho \rangle$ is probably part of unresolved haloes. Most of the gas with these densities is in resolved haloes and has thus been excluded from the plot.

The colour scale in Fig. 5.7 indicates the metal mass weighted mean $\log_{10} m_{\mathrm{halo}}$ as a function of the gas temperature and density for *L050N512* at $z = 0$ (left) and for *L025N512* at $z = 2$ (right). Particles that were never part of a halo containing at least 100 dark matter particles were excluded. These particles account for about 4 and 0.3 percent of the total metal mass in gas at $z = 0$ and 2, respectively. Recall that gas with $\rho \gtrsim 10^2 \langle \rho \rangle$ typically resides in a halo.

There is a strong gradient with density in both panels. The lower the density, the lower the mass of the objects that were responsible for the enrichment. The enrichment of the low-density IGM ($\rho < 10 \langle \rho \rangle$) is dominated by the smallest, resolved haloes, particularly at $z = 0$. This explains the relatively poor convergence that we found for these components in the previous section. Comparing with Fig. 5.2, we see that the low-density photo-ionised IGM ($\rho < 10 \langle \rho \rangle$, $T < 10^{4.5}\mathrm{K}$) is nearly completely missing from Fig. 5.7. This gas phase has therefore only been enriched by haloes below our res-
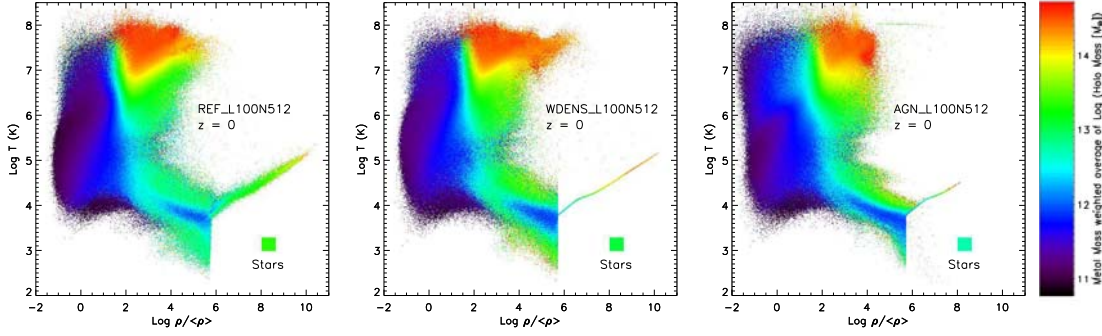
Figure 5.8: As Fig. 5.7 but for simulations *REF_L100N512* (left panel), *WDENS_L100N512* (middle panel), and *AGN_L100N512* (right panel), all at $z = 0$. Model *WDENS* uses an implementation of winds driven by supernovae that is more efficient in massive haloes than the prescription used in model *REF*. Model *AGN* uses the same recipe for supernova feedback as model *REF*, but also includes feedback from AGN. While there are some small differences, the trends are very similar for the three models.

olution limit and/or by intergalactic stars. The latter can occur when stars are ejected from galaxies via some dynamical process and then enrich the ambient IGM.

There is a positive gradient of m_{halo} with T for high densities ($\rho \gtrsim 10^2 \langle \rho \rangle$). Since most of these particles reside in haloes, this merely reflects the fact that the virial temperature is an increasing function of mass.

Fig. 5.8 compares the reference model to model *WDENS*, which uses an implementation of galactic winds that makes them more efficient in high-mass haloes, and to model *AGN*, which includes AGN feedback. While there are some small differences, the trends are identical. Thus, the results are robust to variations in the numerical implementation of galactic winds and to the inclusion of AGN feedback. Henceforth we will therefore only consider the reference model.

Comparison of the left panel of Fig. 5.8 to the left panel of Fig. 5.7, which uses a mass (spatial) resolution that is eight (two) times higher, we see that the trends are also robust with respect to the numerical resolution. However, there are clear quantitative differences (note that the colour scales differ), with the higher resolution simulation giving lower halo masses, particularly for masses near the resolution limit.

Fig. 5.9 shows the metal mass weighted mean $\log_{10}$ of the halo mass that last contained the metals as a function of density (left panel) and temperature (right panel) for *L050N512* at $z = 0$ (black) and for *L025N512* at $z = 2$ (red). This plot therefore shows projections of Fig. 5.7, weighted by the metal mass in each pixel of that figure. The solid curves show the results for all the gas, while the other line styles correspond to cuts in the temperature (left) or density (right). Note that due to the finite resolution of the simulation, we may strongly overestimate the typical halo mass of origin when it is predicted to be of the order the minimum resolved halo mass.

The solid curves in the left panel follow the dot-dashed curves at low densities ($\rho \lesssim 10^2 \langle \rho \rangle$) because most of the metals residing in diffuse gas are hot ($T > 10^{4.5}$ K). Conversely, for densities of order or greater than the star formation threshold, most of the metals are cold and the solid curves follow the dashed curves. We see similar
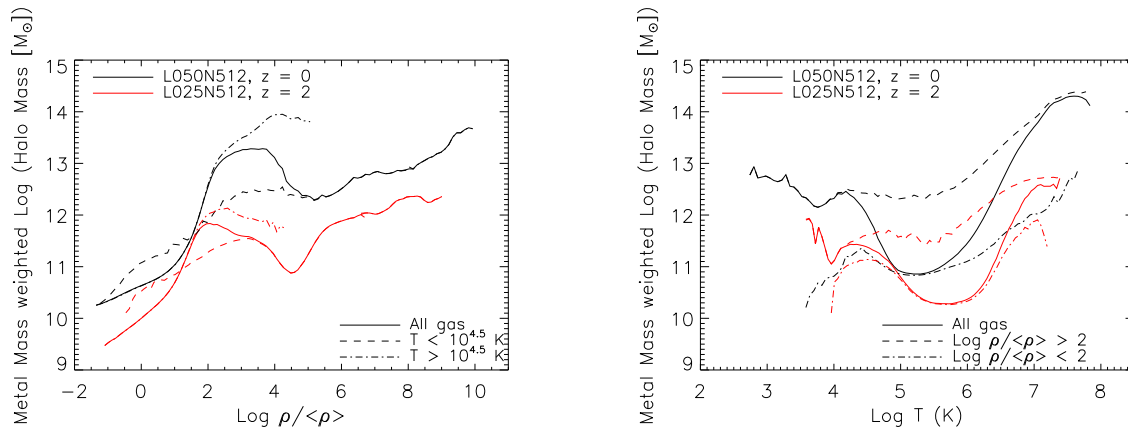
Figure 5.9: Metal mass weighted mean $\log_{10} m_{\mathrm{halo}}$, where m_{halo} is the total mass of the halo that last contained the metals, as a function of the gas density (left panel) or the gas temperature (right panel) at $z = 0$ for model *L050N512* (black) and at $z = 2$ for *L025N512* (red). The different line styles correspond to cuts in the temperature (left panel) or density (right panel) as indicated in the legends. The curves were cut when the number of particles per bin falls below 200. For both the diffuse IGM and the ISM, the typical halo mass that last contained the metals increases with the gas density. Gas at intermediate temperatures ($T \sim 10^5 - 10^6$ K) typically received its metals from lower mass haloes, but this merely reflects the fact that metals at these temperatures reside mostly in lower density gas than metals at lower or higher temperatures, as can be seen by comparing the different line styles in the right panel.

behaviour in the right panel.

The typical halo mass out of which the metals residing in the diffuse IGM were ejected increases strongly with the gas density. As the density increases above that typical of collapsed objects ($\rho \sim 10^2 \langle\rho\rangle$), m_{halo} firsts declines, because cold metals begin to account for a substantial fraction of the metal mass and for lower mass haloes a greater fraction of the gas is in clumps. Beyond the star formation threshold the mean halo mass increases again as more massive haloes sample higher pressure and thus, given our imposed equation of state for star-forming gas, higher density gas. The right panel shows that, for a fixed temperature, metals in higher density gas originate in higher mass haloes. The typical halo mass that last contained the metals reaches a minimum at intermediate temperatures ($T \sim 10^5 - 10^6$ K), because at these temperatures most of the metals reside at low-densities ($\rho < 10^2 \langle\rho\rangle$), while high-density gas dominates the metal content at both low ($T \lesssim 10^4$ K) and high ($T \gtrsim 10^7$ K) temperatures.

In order to gain insight into the distribution of halo masses that contribute to the enrichment of a particular gas phase, we show the cumulative probability distribution function of m_{halo} in Fig. 5.10. Phrased differently, the figure shows the fraction of the metal mass that last resided in halo masses exceeding those plotted along the x-axis. The different columns and line styles correspond to the different regions in $T - \rho$ space shown in Fig. 5.1 and the different colours show the results for different resolutions. The top and bottom rows are for $z = 0$ and $z = 2$, respectively.
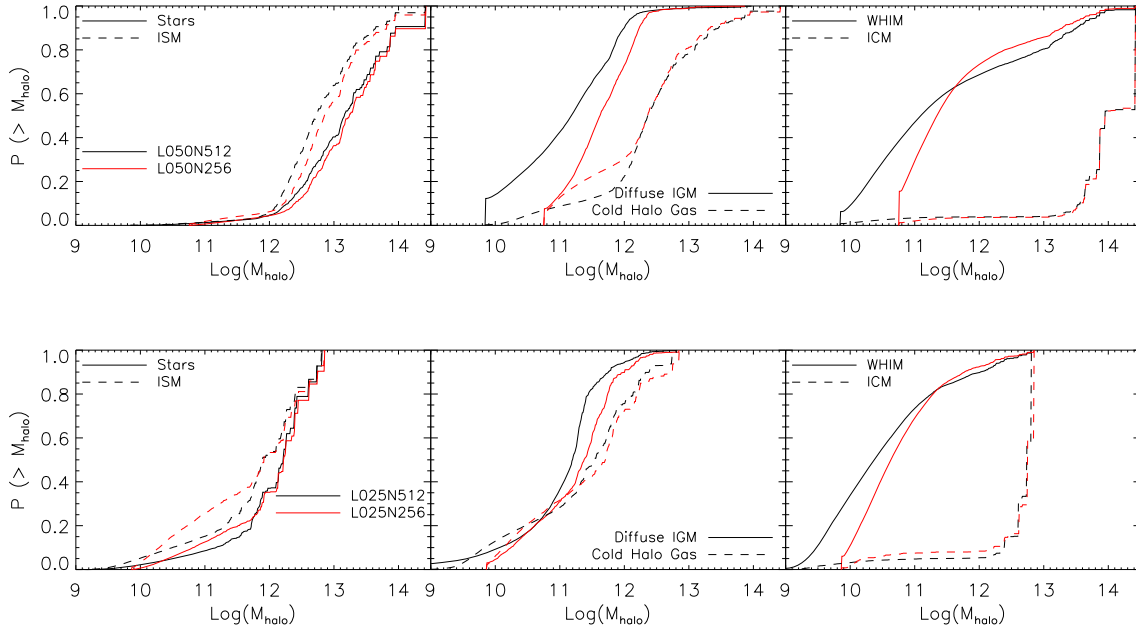
Figure 5.10: Cumulative probability distribution of the halo mass that last contained the metals, weighted by metal mass, at $z = 0$ (top row) and $z = 2$ (bottom row) for stars and for the different gas phases defined in Fig. 5.1. The different colours correspond to different numerical resolutions. For metals that have never resided in a halo with more then 100 dark matter particles we set m_{halo} to the minimum resolved halo mass. The results are close to converged with respect to resolution except for the diffuse IGM and the WHIM. For these phases even our highest resolution runs may overestimate the halo mass. A wide range of halo masses contribute to the enrichment.

For metals that never resided in a resolved halo we set m_{halo} to the dark matter mass of the smallest resolved haloes. The fraction of the metal mass ejected by unresolved haloes is greatest for the diffuse IGM at $z = 0$, for which it is about 12 percent. Comparing the two resolutions, we see that the results for the low-density phases, i.e. the diffuse IGM and the WHIM, are not converged. The situation is worst for the diffuse IGM at $z = 0$. Note that within these phases, convergence will be worse at lower densities as we have already demonstrated that the mean halo mass of origin decreases with decreasing density. Fig. 5.10 clearly shows that a wide range of halo masses contributes to the enrichment of most gas phases. More than half of the metal mass in the diffuse IGM and the WHIM originated from haloes with total mass $M < 10^{11}\,\mathrm{M_\odot}$, which corresponds to stellar masses smaller than $10^9\,\mathrm{M_\odot}$. For the WHIM at $z = 2$ this fraction is about 80%. As we noted in §5.3, if we separate the WHIM at $\rho = 100\langle\rho\rangle$ (not shown), then the low-density component behaves similarly to the full WHIM, while the high-density component is more similar to the ICM.

Finally, Fig. 5.11 shows the fraction of the metal mass that resided in a resolved halo in at least one of our snapshots as a function of the temperature and the density. As we had already observed, most of the metal mass in the colder part of the diffuse IGM
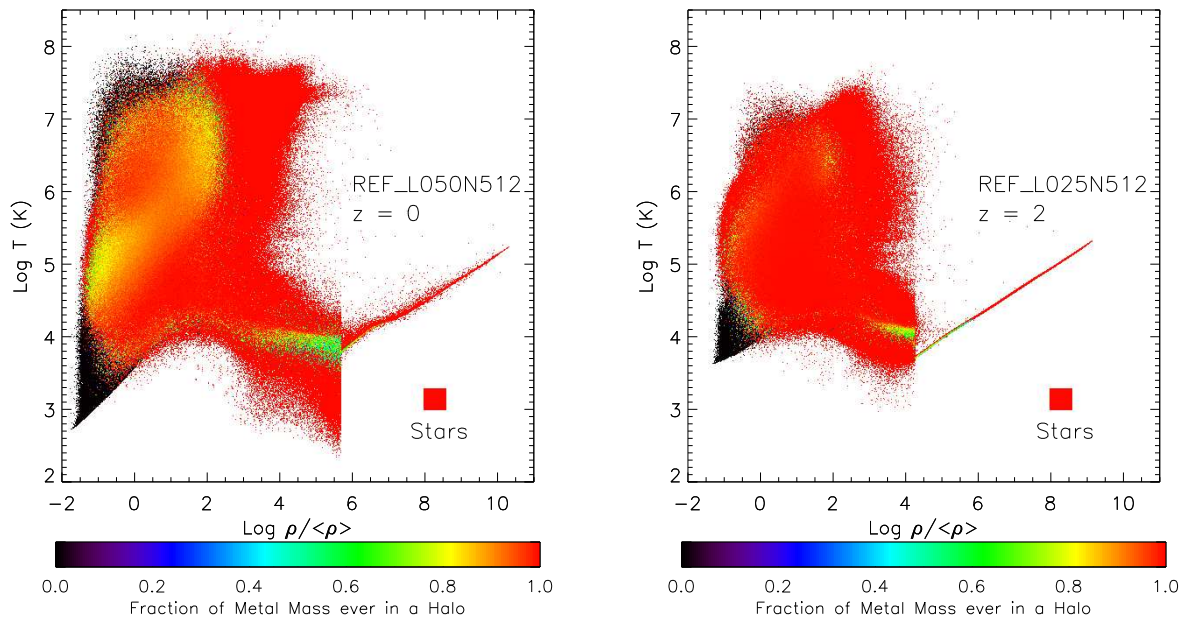
Figure 5.11: Fraction of metal mass that has been in a halo with at least 100 dark matter particles as a function of density and temperature for *L050N512* at $z = 0$ (left panel) and for *L025N512* at $z = 2$ (right panel). Most of the metals in the colder part of the diffuse IGM have never been part of a resolved halo.

has never been part of a resolved halo. The same is true for a small fraction of the cold, dense gas. This reinforces our conclusion that the enrichment of the low-density IGM is dominated by very low-mass haloes with a possible contribution from intergalactic stars.

5.5   WHAT ENRICHED THE IGM AND WHEN?

We conclude by simultaneously addressing the two questions that we investigated in the two previous sections: When was the IGM enriched and by what? Fig. 5.12 shows the metal mass distribution as a function of both z_Z and m_{halo} for model *L050N512* at $z = 0$ (left column) and for model *L025N512* at $z = 2$ (right column). The top and bottom rows show the results for metals residing in the diffuse IGM and the WHIM, respectively. Metals that are currently part of a halo were excluded (note that this corresponds to a large fraction of the metals for the case of the WHIM). As discussed before, the finite resolution of our simulations will cause us to underestimate the importance of haloes with masses near and below the minimum halo mass that we consider.

Focusing first on the diffuse IGM at $z = 0$ (the top-left panel of Fig. 5.12), we see that there is a strong anti-correlation between the enrichment redshift and the mass of the halo from which the metals were ejected. Early enrichment is more strongly dominated by lower mass galaxies. For metals residing in the diffuse IGM at $z = 2$ (top-right panel) this is also the case, but the enrichment seems to have been dominated by objects with $m_{halo} \sim 10^{11}\,\mathrm{M_\odot}$ (which corresponds to a stellar mass $m_* \sim 10^9\,\mathrm{M_\odot}$), which
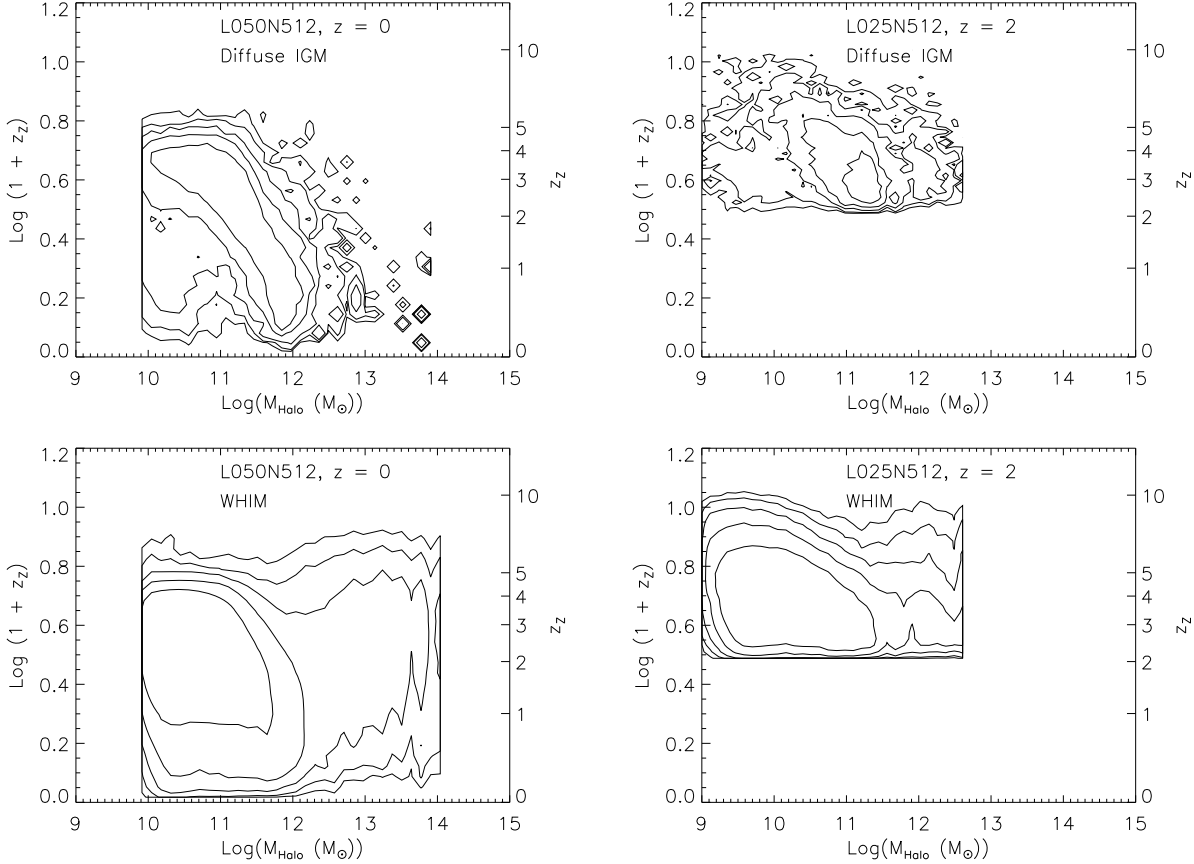
Figure 5.12: Distribution of metal mass as a function of m_{halo}, the metal mass weighted mean mass of the last resolved halo that contained the metals, and z_Z, the metal mass weighted mean enrichment redshift. Results are shown for the diffuse IGM (top row) and the WHIM (bottom row) at $z = 0$ for *L050N512* (left column) and at $z = 2$ for *L025N512* (right column). The contours are logarithmically spaced by 0.5 dex. Metals that are currently in a halo and metals that have never been part of a resolved halo were both excluded. Older metals were typically ejected by lower mass haloes, particularly if they end up in the diffuse IGM. The WHIM was enriched by a wide range of halo masses.

is about two orders of magnitude greater than the minimum halo mass we consider. The smaller role for the lowest mass haloes at $z = 2$ is also apparent from a comparison of the solid curves in the middle panels of Fig. 5.10. It appears that the resolution of the *L025N512* simulation is nearly sufficient to model the enrichment of the diffuse IGM at $z = 2$.

We must keep in mind, however, that the diffuse IGM is not a single phase. We have already demonstrated that z_Z and m_{halo} are strongly increasing resp. decreasing functions of the gas density (see Figs. 5.4 and 5.9). For example, for the diffuse IGM at $z = 2$ the metal mass weighted mean $\log_{10} m_{halo}$ decreases from ≈ 12 for an overdensity of 10^2 to ≈ 10 (i.e. too close to the resolution limit to be converged) at the mean density.

It is likely that a significant fraction of the metal mass that resides at the high-density end of the diffuse IGM at $z = 2$, which is typically ejected by more massive

haloes, will have fallen back into haloes by $z = 0$ and will therefore no longer be part of the diffuse IGM. This effect can help explain why m_{halo} is smaller at $z = 0$ than at $z = 2$ and why there is an anti-correlation between z_Z and m_{halo}. Evolution of the halo mass function is likely also an important part of the explanation. At higher redshifts the masses of the haloes producing metals are typically lower.

The enrichment history of the WHIM (bottom row of Fig. 5.12) shows some interesting differences from that of the diffuse IGM. At $z = 0$ the anti-correlation between z_Z and m_{halo} is much weaker. Relatively recent enrichment by low-mass haloes is more important for the WHIM. Presumably, metals that are ejected recently are shock-heated by the winds that carry them and many of them may not have had sufficient time to cool down to the temperatures of the diffuse IGM. High-mass haloes are also more important for the WHIM. This may largely be because high-mass haloes tend to be embedded in gas that is heated by gravitational accretion shocks and is therefore sufficiently hot to be considered part of the WHIM.

The results for the other OWLS models considered here are very similar (not shown), although higher mass haloes are slightly more important for *WDENS* and *AGN*, presumably because in these models feedback is more efficient in such objects.

5.6 CONCLUSIONS

We have used cosmological, hydrodynamical simulations that include radiative cooling, star formation, stellar evolution and supernova feedback, and, in some cases, AGN feedback, to investigate the metal enrichment history of the Universe. Specifically, we took advantage of the Lagrangian nature of our simulations to investigate when gas that ends up in a particular gas phase at redshift $z = 0$ or $z = 2$ received its metals and what the masses were of the haloes that last contained these metals.

We considered different physical models, all taken from the OWLS project, including simulations with a different implementation of supernova feedback and a model that includes AGN feedback. While there are some small differences, such as slightly higher enrichment redshifts for models with more efficient feedback in massive galaxies, the main trends are strikingly similar for all models. Although we cannot rule out that some of our conclusions may depend on the details of our method (e.g. the use of SPH), the similarities between different feedback models suggest that our conclusions are robust.

The time since the enrichment varies most strongly with the gas density. Metals in lower density gas are typically much older than metals in high-density gas, a trend that extends over ten orders of magnitude in gas density. At least half of the metals that reside in the diffuse IGM at $z = 0$ ($z = 2$) were ejected above redshift two (three).

The enrichment redshift also varies with the temperature of the gas, but this mostly reflects the fact that the typical gas density of enriched gas varies with its temperature. For gas that is dense enough to be able to cool, the time since enrichment correlates well with the cooling time. Gas with shorter cooling times received its metals more recently.

The typical mass of the haloes from which the metals residing in the IGM were

ejected, increases rapidly with the gas density. At least half of the metal mass was ejected by haloes with total masses less than $10^{11}\,M_\odot$, which corresponds to stellar masses smaller than $10^9\,M_\odot$. For the low-redshift IGM the mass of the dominant IGM polluters may be substantially smaller than this because our predictions for present day low-density gas are not close to converged with respect to the numerical resolution.

The age of the metals ending up in the diffuse IGM is strongly anti-correlated with the mass of the haloes from which they were ejected. In other words, older metals were typically ejected by lower mass haloes. This anti-correlation is less strong for the hotter part of the IGM (the WHIM), for which recent enrichment by low-mass haloes is more important. While massive haloes ($> 10^{12}\,M_\odot$) are unimportant for the enrichment of the diffuse IGM, they do contribute to the pollution of the warm-hot IGM at low redshift.

Our main and strongest conclusion is that metals residing in lower density gas were typically ejected earlier and by lower mass haloes. This suggests that travel-time is a limiting factor for the enrichment of the IGM, as proposed by Aguirre et al. (2001b). Metals that have been ejected recently simply have not had sufficient time to reach the low-density gas far from galaxies. The anti-correlation between metal age and halo mass would then follow because typical galaxy masses are lower at higher redshifts. Another mechanism that could explain the trends is fall back onto galaxies. If metals ejected by lower mass galaxies are less likely to fall back (e.g. Oppenheimer et al. 2009) or if they typically leave the haloes with larger velocities, then we would expect lower mass galaxies to be more important for gas that is further away. Finally, low-mass galaxies are more weakly clustered than high-mass galaxies, thus low-density gas is more accessible to low-mass galaxies.

It is not immediately obvious how one could compare this result with observations. One way would be to consider abundance ratios of elements in various phases as a function of density and redshift in an attempt to find a signature that could be searched for in high-redshift observations. However, uncertainties in the nucleosynthetic yields and the type Ia supernova rates (see chapter 3), as well as in the ionization corrections, may make such a comparison troublesome. Correlations between absorbers and the distances to different types of galaxies may also help shed light on the enrichment mechanism (e.g. Steidel et al. 2010; Chen & Mulchaey 2009; Wilman et al. 2007; Stocke et al. 2006), although is is important to keep in mind that the metals that are observed to be near a galaxy may have been injected by its lower-mass progenitors (Porciani & Madau 2005; Scannapieco 2005). In fact, our results would imply that this is likely to be the case for metals in low-density gas. We leave an analysis of abundance ratios and other observational comparisons to a future work.

The importance of low-mass galaxies is a challenge for simulations of the enrichment of the IGM, as it implies the need for high-resolution in large volumes. On the other hand, our results suggest that the low-density IGM provides us with an exciting opportunity to study the consequences of feedback in low-mass galaxies, a key but poorly understood ingredient of models of galaxy formation, and that it provides us with a fossil record of galaxy formation in the high-redshift Universe.

Acknowledgements

References

Agertz O., Moore B., Stadel J., Potter D., Miniati F., Read J., Mayer L., Gawryszczak A., Kravtsov A., Nordlund Å., Pearce F., Quilis V., Rudd D., Springel V., Stone J., Tasker E., Teyssier R., Wadsley J., Walder R., 2007, MNRAS, 380, 963

Aguirre A., Dow-Hygelund C., Schaye J., Theuns T., 2008, ApJ, 689, 851

Aguirre A., Hernquist L., Schaye J., Katz N., Weinberg D. H., Gardner J., 2001a, ApJ, 561, 521

Aguirre A., Hernquist L., Schaye J., Weinberg D. H., Katz N., Gardner J., 2001b, ApJ, 560, 599

Aguirre A., Schaye J., Hernquist L., Kay S., Springel V., Theuns T., 2005, ApJ, 620, L13

Aracil B., Petitjean P., Pichon C., Bergeron J., 2004, A&A, 419, 811

Booth C. M., Schaye J., 2009, MNRAS, 398, 53

Borgani S., Fabjan D., Tornatore L., Schindler S., Dolag K., Diaferio A., 2008, Space Science Reviews, 134, 379

Cen R., Ostriker J. P., 1999, ApJ, 519, L109

Chabrier G., 2003, PASP, 115, 763

Chen H., Mulchaey J. S., 2009, ApJ, 701, 1219

Choi J., Nagamine K., 2010, ArXiv e-prints

Cooksey K. L., Thom C., Prochaska J. X., Chen H., 2010, ApJ, 708, 868

Cowie L. L., Songaila A., 1998, Nature, 394, 44

Dalla Vecchia C., Schaye J., 2008, MNRAS, 387, 1431

Danforth C. W., Shull J. M., 2008, ApJ, 679, 194

Davé R., Oppenheimer B. D., 2007, MNRAS, 374, 427

Ellison S. L., Songaila A., Schaye J., Pettini M., 2000, AJ, 120, 1175

Ferland G. J., Korista K. T., Verner D. A., Ferguson J. W., Kingdon J. B., Verner E. M., 1998, PASP, 110, 761

Gnat O., Sternberg A., 2007, ApJS, 168, 213

Haardt F., Madau P., 2001, in Neumann D. M., Tran J. T. V., eds, Clusters of Galaxies and the High Redshift Universe Observed in X-rays Modelling the UV/X-ray cosmic background with CUBA

Jarosik N., Bennett C. L., Dunkley J., et al., 2010, ArXiv e-prints

Kawata D., Rauch M., 2007, ApJ, 663, 38

Kobayashi C., Springel V., White S. D. M., 2007, MNRAS, 376, 1465

Madau P., Ferrara A., Rees M. J., 2001, ApJ, 555, 92

Marigo P., 2001, A&A, 370, 194

McCarthy I. G., Schaye J., Ponman T. J., et al., 2009, arXiv:0911.2641

Mitchell N. L., McCarthy I. G., Bower R. G., Theuns T., Crain R. A., 2009, MNRAS, 395, 180

Oppenheimer B. D., Davé R., 2006, MNRAS, 373, 1265

Oppenheimer B. D., Davé R., 2008, MNRAS, 387, 577

Oppenheimer B. D., Davé R., 2009, MNRAS, 395, 1875

Oppenheimer B. D., Davé R., Kereš D., Fardal M., Katz N., Kollmeier J. A., Weinberg D. H., 2009, ArXiv e-prints

Pieri M. M., Frank S., Mathur S., Weinberg D. H., York D. G., Oppenheimer B. D., 2009, ArXiv:0908.2001

Porciani C., Madau P., 2005, ApJ, 625, L43

Portinari L., Chiosi C., Bressan A., 1998, A&A, 334, 505

Scannapieco E., 2005, ApJ, 624, L1

Scannapieco E., Pichon C., Aracil B., Petitjean P., Thacker R. J., Pogosyan D., Bergeron J., Couchman H. M. P., 2006, MNRAS, 365, 615

Schaye J., 2004, ApJ, 609, 667

Schaye J., Aguirre A., Kim T.-S., Theuns T., Rauch M., Sargent W. L. W., 2003, ApJ, 596, 768

Schaye J., Carswell R. F., Kim T., 2007, MNRAS, 379, 1169

Schaye J., Dalla Vecchia C., 2008, MNRAS, 383, 1210

Schaye J., Dalla Vecchia C., Booth C. M., et al., 2010, MNRAS, 402, 1536

Schaye J., Rauch M., Sargent W. L. W., Kim T.-S., 2000, ApJ, 541, L1

Shen S., Wadsley J., Hayfield T., Ellens N., 2010, MNRAS, 401, 727

Sheth R. K., Mo H. J., Tormen G., 2001, MNRAS, 323, 1

Simcoe R. A., Sargent W. L. W., Rauch M., 2004, ApJ, 606, 92

Sommer-Larsen J., Fynbo J. P. U., 2008, MNRAS, 385, 3

Springel V., 2005, MNRAS, 364, 1105

Steidel C. C., Erb D. K., Shapley A. E., Pettini M., Reddy N. A., Bogosavljević M., Rudie G. C., Rakic O., 2010, ArXiv e-prints

Stocke J. T., Penton S. V., Danforth C. W., Shull J. M., Tumlinson J., McLin K. M., 2006, ApJ, 641, 217

Sutherland R. S., Dopita M. A., 1993, ApJS, 88, 253

Theuns T., Viel M., Kay S., Schaye J., Carswell R. F., Tzanavaris P., 2002, ApJ, 578, L5

Thielemann F.-K., Argast D., Brachwitz F., et al., 2003, in From Twilight to Highlight: The Physics of Supernovae Supernova Nucleosynthesis and Galactic Evolution. pp 331–+

Tornatore L., Borgani S., Matteucci F., Recchi S., Tozzi P., 2004, MNRAS, 349, L19

Tornatore L., Borgani S., Viel M., Springel V., 2010, MNRAS, 402, 1911

Wilman R. J., Morris S. L., Jannuzi B. T., Davé R., Shone A. M., 2007, MNRAS, 375, 735